Nanoscale

PAPER

View Article Online
View Journal | View Issue

Cite this: *Nanoscale*, 2024, **16**, 9496

Gallic acid-loaded HFZIF-8 for tumor-targeted delivery and thermal-catalytic therapy†

Xing Yang,[a,c] Chunsheng Li,[a] Shuang Liu,[a] Yunlong Li,[a] Xinyu Zhang,[a] Qiang Wang,[a] Jin Ye,[a] Yong Lu,[a,c,d] Yujie Fu[b] and Jiating Xu *[a,b,c]

"Transition" metal-coordinated plant polyphenols are a type of promising antitumor nanodrugs owing to their high biosafety and catalytic therapy potency; however, the major obstacle restricting their clinical application is their poor tumor accumulation. Herein, Fe-doped ZIF-8 was tailored using tannic acid (TA) into a hollow mesoporous nanocarrier for gallic acid (GA) loading. After hyaluronic acid (HA) modification, the developed nanosystem of HFZIF-8/GA@HA was used for the targeted delivery of Fe ions and GA, thereby intratumorally achieving the synthesis of an Fe-GA coordinated complex. The TA-etching strategy facilitated the development of a cavitary structure and abundant coordination sites of ZIF-8, thus ensuring an ideal loading efficacy of GA (23.4 wt%). When HFZIF-8/GA@HA accumulates in the tumor microenvironment (TME), the framework is broken due to the competitive protonation ability of overexpressed protons in the TME. Interestingly, the intratumoral degradation of HFZIF-8/GA@HA provides the opportunity for the *in situ* "meeting" of GA and Fe ions, and through the coordination of polyhydroxyls assisted by conjugated electrons on the benzene ring, highly stable Fe-GA nanochelates are formed. Significantly, owing to the electron delocalization effect of GA, intratumorally coordinated Fe-GA could efficiently absorb second near-infrared (NIR-II, 1064 nm) laser irradiation and transfer it into thermal energy with a conversion efficiency of 36.7%. The photothermal performance could speed up the Fenton reaction rate of Fe-GA with endogenous H_2O_2 for generating more hydroxyl radicals, thus realizing thermally enhanced chemodynamic therapy. Overall, our research findings demonstrate that HFZIF-8/GA@HA has potential as a safe and efficient anticancer nanodrug.

Received 14th March 2024,
Accepted 10th April 2024

DOI: 10.1039/d4nr01102c

rsc.li/nanoscale

Introduction

Natural plant polyphenols[1–3] have received wide attention in the antitumor field on account of their low burden on the human body[4–6] and multiple mechanisms for cancer treatment.[7–9] Gallic acid (GA), as one of the most common natural polyphenols,[10,11] is important in the anticancer field because of its selective cytotoxicity to various kinds of cancer cells.[12,13] GA exerts its effects through different pharmacological and biochemical pathways, which could provide strong antioxidation, anti-inflammatory, antimutation, and anticancer effects, as well as concentration-dependent pro-oxidation characteristics in the metal-ion environment.[14] Specially, benefiting from the pro-oxidation properties of GA, it has been recognized as a death inducer in cancer cell lines. Nevertheless, its poor water solubility and lack of tumor targeting ability have seriously affected the therapeutic effect of GA.

It is reported that GA can self-assemble with metal ions to form a metal–polyphenol network structure using the phenolic hydroxyl group in GA as the chelating site for not only improving biocompatibility and sensitivity in the tumor microenvironment (TME), but also for keeping the intrinsic biological activities of polyphenols.[15–18] In addition, metal–polyphenol nanocomposites with additional properties can be constructed by combining metal ions, for instance, Fe, Mn, and Cu, with polyphenol materials.[19–22] Among these metal ions, Fe^{2+} is a very promising metal ion that can kill tumor cells *via* the Fenton reaction.[23–25] Moreover, the Fe-GA complex formed by the coordination of Fe and GA exhibits intense second near-infrared (NIR-II) absorption because of the strong delocalization in the π-electron structure, which is regarded as an efficient photothermal therapy (PTT) agent.[26,27] Meanwhile, the coordination complex of Fe-GA is able to cause cancer cell death by the synergistic treatment of chemodynamic therapy

[a]*Laboratory of Forest Plant Ecology, Ministry of Education, College of Chemistry, Chemical Engineering and Resource Utilization, Northeast Forestry University, Harbin 150040, P. R. China. E-mail: xujiating66@163.com*
[b]*College of Forestry, Beijing Forestry University, Beijing 100083, P. R. China*
[c]*Heilongjiang Provincial Key Laboratory of Ecological Utilization of Forestry-Based Active Substances, Northeast Forestry University, Harbin, 150040, P. R. China*
[d]*School of Laboratory Medicine, Wannan Medical College, Wuhu, Anhui 241002, P. R. China*

†Electronic supplementary information (ESI) available. See DOI: https://doi.org/10.1039/d4nr01102c

(CDT) and PTT.[28–30] For instance, Tian *et al.* used bovine serum albumin, Fe ions, and GA to prepare an Fe-GA coordination complex with a hollow structure for multimodal therapy.[25] Thereafter, Dong *et al.* constructed an Fe-polyphenol nanovaccine for tumor immunotherapy and CDT.[28] However, this could be easily metabolized and excreted in the living body due to lacking the effective delivery mechanism for Fe-GA intratumorally.[31] Therefore, there is an urgent need to develop a highly delivery system for transporting the Fe-GA coordination complex into tumor cells intratumorally.

Zeolite imidazolate frame-8 (ZIF-8), a subclass of organometallic framework composed by Zn ions and 2-methylimidazole (2-MeIM), has been widely explored as a carrier in the cancer therapy field due to its high biocompatibility, pH-responsiveness, adjustable components, diverse structures, and drug-loading potency.[32–38] For example, Zheng and coworkers reported ZnO-DOX@ZIF-8 nanoparticles using ZnO as a zinc source to coordinate with the 2-methylimidazoline ligand and then loaded the chemotherapy drug DOX for antitumor application.[39] Besides, Ma *et al.* designed a new type of TME-responsive therapeutic nanosystem of Co/ZIF-8/ICG/Pt for photodynamic therapy and CDT.[40] Therein, the ZIF-8 served as the carrier for the TME-responsive therapeutic nanoplatform, and was loaded with the photosensitizer indocyanine green while incorporating Co ions into its own skeleton structure. However, the application of bulk ZIF-8 in the anticancer field is limited by its small pore size and low loading efficiency for drugs. Thus, researchers are increasingly focusing on developing ZIF-8 with larger pore diameters, especially with hollow structures. Recently, many kinds of ZIF-8 with hollow structures (HZIF-8) have been reported due to their high dispersibility, low density, and high drug-loading capacity, providing a huge opportunity for assembling with mostly hybrid phases for anticancer applications.[41–45] For instance, Zhou *et al.* loaded CuS nanoparticles in Au-doped HZIF-8, which showed a higher loading capacity than that of traditional ZIF-8, and displayed a larger pore size to facilitate drug loading.[46] Alternatively, Wang *et al.* prepared HZIF-8/PDA as a nanocarrier for cyclodextrins and hydrophobic drugs to treat cancer through the synergistic effect of PTT and CDT.[47] However, these reported hollow ZIF-8 materials could not stably anchor the drug molecules, resulting in a certain degree of premature leakage of the loaded drugs during *in vivo* circulation, and thus compromising the final tumor killing effect.[48,49]

In this contribution, to solve the above problems, we prepared a hollow Fe-doped ZIF-8 with GA loading and hyaluronic acid (HA) modification (noted as HFZIF-8/GA@HA) by a two-step strategy for PTT-enhanced catalytic therapy. In detail, Fe ions were doped into a cubic-structural ZIF-8 constructed by the coordination of Zn ions, cetyltrimethyl ammonium bromide (CTAB), and 2-MeIM. The Fe^{2+} ions replaced part of the Zn^{2+} ions in the framework of ZIF-8 to provide more binding sites for loading GA and endow the HZIF with Fe^{2+} ions for a more potent Fenton reaction. In addition, after the HFZIF-8/GA is degraded in the TME, the released Fe^{2+} ions can not only self-assemble with GA to form Fe-GA complexes but can also catalyze endogenous H_2O_2 to hydroxyl radicals. Here, the Fe-doped ZIF-8 (FZIF-8) was etched by tannic acid (TA) to form nanocubes with hollow mesoporous pores. Subsequently, the hollow FZIF-8 (HFZIF-8) was loaded with GA and modified with HA, which endowed the nanoparticles with a targeting effect for the TME. HFZIF-8/GA@HA showed a high load efficiency for GA and good photothermal conversion efficacy with a 1064 nm laser, thus generating intratumoral Fe-GA complexes to realize synergetic CDT/PTT. Benefiting from the targeting role of HA and acidity sensitivity of the nanoparticles in the TME, HFZIF-8/GA@HA demonstrated a high cell uptake rate in tumor cells, enabling the intratumoral Fe-GA complex to be efficiently formed for hyperthermia-enhanced catalytic therapy.

Results and discussion

Chemical synthesis and structure characterization

The synthetic procedures related to HFZIF-8/GA@HA and the catalytic mechanism of hyperthermia-enhanced catalytic therapy are illustrated in Scheme 1. In detail, a limited number of protons were offered by TA, which can chelate ions of the metal to accelerate etching, thereby disclosing more active sites (Fig. S1†).[50] In contrast to previous reports on HZIF-8, HFZIF-8/GA@HA has some merits for potentiating cancer theranostics: (i) FZIF-8 can be degraded in an acidic environment to achieve the formation of Fe-GA (the coordination structure of Fe-GA is supplied in Scheme 1); (ii) Fe-GA provides for an efficient Fenton reaction *via* continuously producing a large amount of hydroxyl radicals ($^{\bullet}OH$); (iii) Fe-GA has an obvious photothermal effect, thus further killing tumor cells by photothermal-enhanced CDT. To sum up, HFZIF-8/GA@HA can realize a high catalytic therapy effect to restrain tumor growth based on reactive oxygen species (ROS).

Scanning electron microscopy (SEM) and transmission electron microscopy (TEM) analyses revealed the shape and morphology of the as-synthesized nanoparticles. As illustrated in Fig. 1a, c and Fig. S3,† FZIF-8 had a cubic morphology with an average diameter of about 150 nm. As shown in Fig. S4,† the hydrodynamic diameter of FZIF-8 (154 nm) was slightly larger than the size in the TEM images, which was attributed to the formation of hydration layers on the surface of the particles. Meanwhile, the SEM and TEM images of ZIF-8 are respectively displayed in Fig. S2a and S2b,† where it could be observed that Fe-doping did not destroy the cubic structure of ZIF-8. The framework of HFZIF-8 etched by TA exhibited an obvious hollow structure, in which cavities with an average diameter and shell thickness of 120 nm and 30 nm could be observed, respectively (Fig. 1b and d). In addition, HFZIF-8 displayed a hydrodynamic diameter of 158 ± 12.8 nm (Fig. S4†), which was consistent with the result from TEM. Obviously, compared to FZIF-8, the surface of HFZIF-8 with cavities seemed to be rougher due to the TA etching. The corresponding element composition and distribution were revealed by elemental mapping (Fig. 1e). At the same time, the element contents of

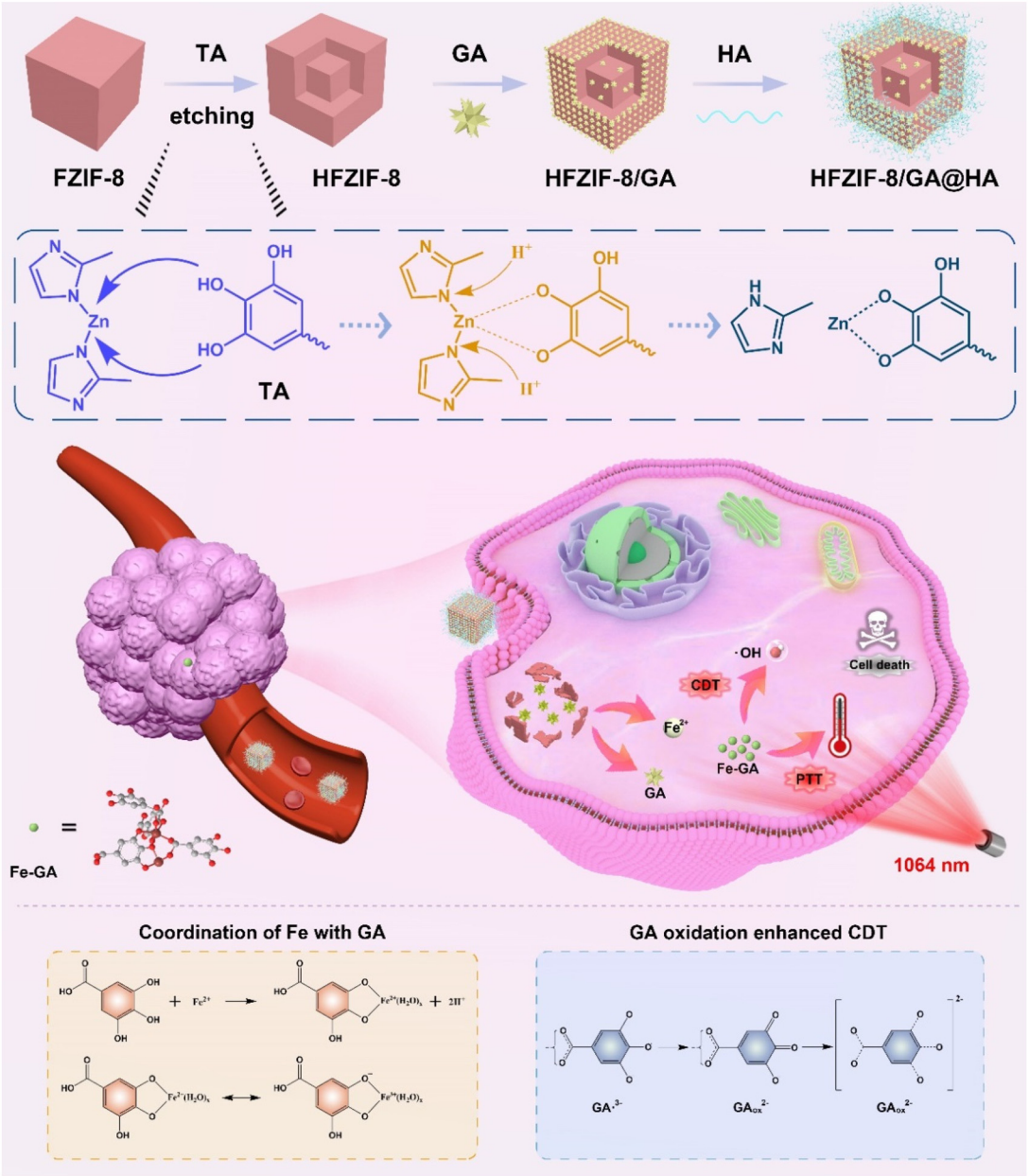

Scheme 1 Schematic illustration for the preparation of HFZIF-8/GA@HA and the simulative mechanism of HFZIF-8/GA@HA for synergetic PTT-enhanced catalytic therapy.

Zn and Fe were 2.69% and 0.35%, respectively (Fig. 1e and Fig. S5†). It was especially noteworthy that other elements were not observed across the entire nanostructure except for C, N, Zn, Fe, and O, which also proved that Fe atoms were only distributed in hollow FZIF-8. To further verify the effect of doping Fe and TA etching on the structure of FZIF-8, X-ray diffraction (XRD) was employed. The results showed that FZIF-8 was consistent with ZIF-8's simulated standard card, indicating the doping of Fe and the etching of TA did not affect the crystal structure of ZIF-8 (Fig. 1f).

Next, Brunauer–Emmett–Teller (BET) analysis was employed to test the specific surface area and pore size of FZIF-8 before and after HFZIF-8 was etched by TA. Notably, FZIF-8 had an obvious mesoporous structure, and the average and main pore sizes were 2.1 nm and 1.5 nm, respectively (Fig. S6†). After FZIF-8 was etched by TA, the specific surface area of HFZIF-8 decreased from 1138.6 $cm^2\ g^{-1}$ to 114.6 $cm^2\ g^{-1}$, and the average pore size increased from 2.1 nm to 18.6 nm (Fig. 1g). Meanwhile, the main pore size increased from 1.5 nm to 1.8 nm. Because of its wide surface area and unique mesoporous structure, HFZIF-8 has more exposed active sites for efficient catalysis, which is advantageous for GA loading.

To demonstrate the successful loading of GA and rational decoration of HA, the prepared HFZIF-8/GA and HFZIF-8/

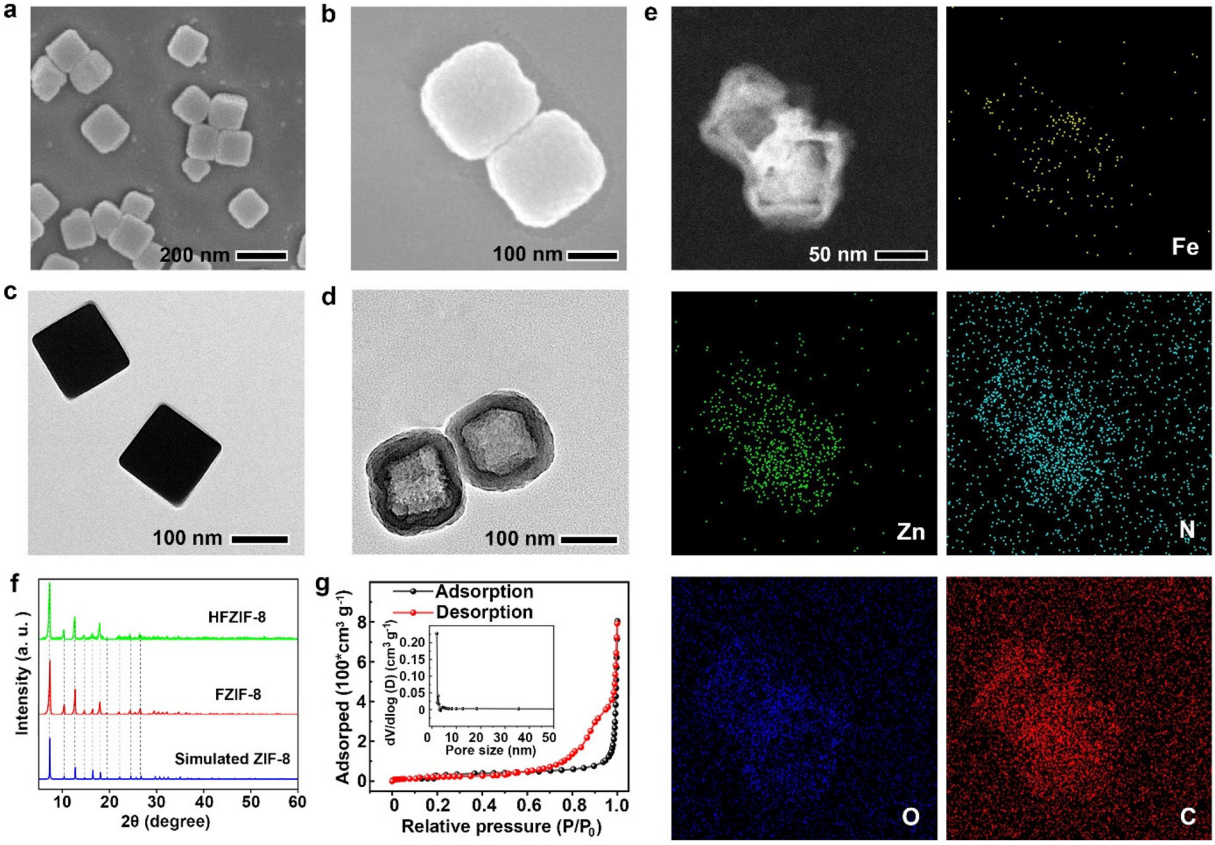

Fig. 1 SEM images of the Fe-doped ZIF-8 (a) and HFZIF-8 (b). TEM images of the Fe-doped ZIF-8 (c), and HFZIF-8 (d). HAADF-STEM image and EDS element mappings of Fe, Zn, N, O, and C (e). XRD patterns of the Fe-doped ZIF-8, HFZIF-8, and simulated cards of ZIF-8 (f). N_2 absorption–desorption isotherm and corresponding pore-size distribution for HFZIF-8 (g).

GA@HA were characterized by Fourier transform near-infrared (FT-IR) spectroscopy. In Fig. 2a, the peaks in the range of 2900–3200 cm^{-1} belonged to the N–H and C–H stretching vibrations of the methyl and primary amine groups of FZIF-8. The peak at 421 cm^{-1} was attributed to the stretching vibration of Zn–N bond.[44] The characteristic peaks at 1265 cm^{-1} (C–O stretching) and 1026 cm^{-1} (O–H in-plane deformation) confirmed that GA was successfully loaded into HFZIF-8, while the peaks at 1331 cm^{-1} (C–O), 1737 cm^{-1} (C═O), and 1633 cm^{-1} (C═C) also further proved the successful loading of GA. As expected, the peaks of HFZIF-8/GA@HA at 1640 cm^{-1} (CO-NH) and 677 cm^{-1} (CO-NH) indicated that HFZIF-8 was successfully modified by HA.[51–53]

The decreased potential of HFZIF-8/GA@HA further supported the above results *via* zeta potential analysis (Fig. S7a†). Besides, the stability of HFZIF-8 in neutral solution was also proved by the zeta (ζ) potential analysis over 7 days (Fig. S7b†). Also, we detected the UV–vis absorption spectrum of the centrifugal supernatant after HA modification (Fig. S8†), in which no characteristic peak of GA was detected. Therefore, the leakage of GA in the HA modification process can be almost ignored.

Also, the UV–vis absorption spectra of HFZIF-8, HFZIF-8/GA, and HFZIF-8/GA@HA were studied by diffuse reflectance UV–vis absorption spectroscopy (DR-UV–vis) (Fig. S9a and S9b†). The UV–vis absorption peak of GA showed a red-shift in HFZIF-8/GA, which was attributed to the coordination of some GA with Fe^{2+} ions in HFZIF-8. Obviously, a certain absorbance peak at 1064 nm could be observed in the spectrum of HFZIF-8/GA@HA, which provided a good potential for PTT for the nanosystem (Fig. S10†). At same time, the loading rate of GA was calculated through the UV–vis absorption spectra of GA with various concentrations and the standard curve of GA (Fig. S11a and S11b†). Therefore, the loading rate in HFZIF-8/GA was increased to 23.4 wt%. By contrast, compared with HFZIF-8, the loading rate of GA in ZIF-8 was only 14.1 wt% (Fig. S11c and S11d†). Next, X-ray photoelectron spectroscopy (XPS) was employed to further evaluate the composition of elements in HFZIF-8, and the results are shown in Fig. 2b. The peaks of Zn 2p, Fe 2p, N 1s, O 1s, and C 1s could be completely observed in the spectrum of HFZIF-8. Simultaneously, the high-resolution spectrum of Fe 2p indicated the presence of Fe^{2+} (710.89 eV) and Fe^{3+} (710.74 eV) in HFZIF-8 (Fig. 2c). The spectra of Zn $2p_{1/2}$ (1043.17 eV) and $2p_{2/3}$ (1020.64 eV) confirmed the existence of Zn^{2+} (Fig. S12†).[26,30]

Chemodynamic therapy

The presence of Fe^{2+} endowed HFZIF-8/GA with the ability to catalyze H_2O_2 decomposition and produce $^{\bullet}OH$ by the Fenton

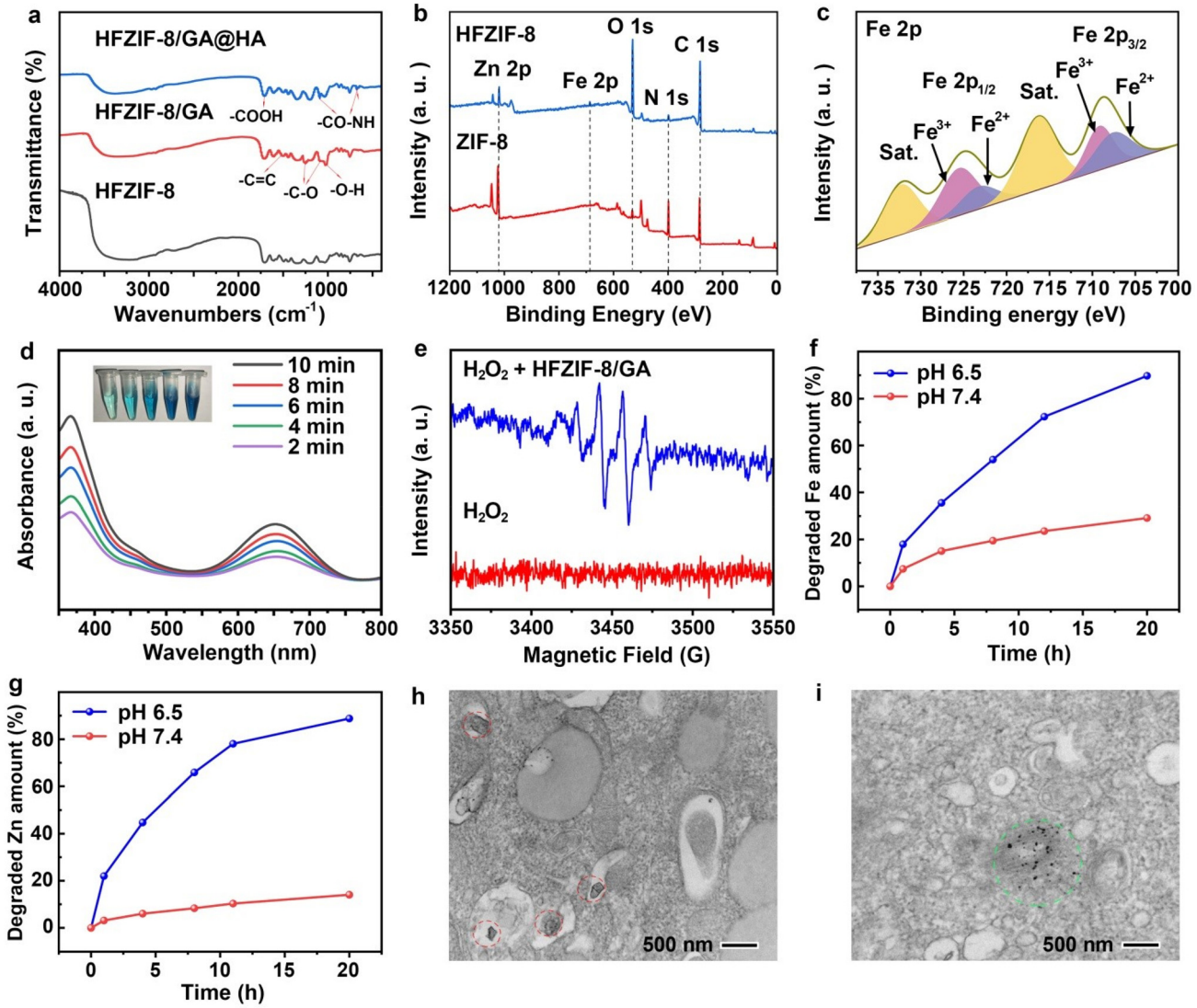

Fig. 2 FT-IR spectra of HFZIF-8, HFZIF-8/GA, and HFZIF-8/GA@HA (a). XPS survey spectra of Fe-doped ZIF-8 and HFZIF-8 (b). High-resolution XPS spectrum of Fe 2p in HFZIF-8 (c). TMB degradation curves of HFZIF-8/GA degradation products plus H_2O_2 (1 mM) by the $^{\bullet}OH$ produced at various times (pH 6.5) (d). ESR spectra for detection of the $^{\bullet}OH$-generation ability of HFZIF-8/GA by DMPO after degradation (e). Accumulated release curves of Fe (f) and Zn (g) elements from HFZIF-8 in different PBS solutions. Bio-TEM images of HeLa cells incubated with HFZIF-8/GA@HA for 1 h (h) and 12 h (i).

reaction under hypoxic conditions.[54] To verify that HFZIF-8/GA could be used as a CDT agent to produce reactive oxygen species (ROS), methyl orange (MO) and 3,3′,5,5′-tetramethylbenzidine (TMB) were employed for ROS detection. The degradation of MO could prove the occurrence of the Fenton reaction based on Fe-GA. In addition, the significantly increased absorbance of TMB at 654 nm could indicate the prominent ROS generation of HFZIF-8/GA treated with H_2O_2. As shown in Fig. S13a,† when the contents of HFZIF-8/GA were varied from 0 to 1 mg ml^{-1} under the acid conditions, the MO degradation capacity of HFZIF-8 was gradually elevated, which was ascribed to the existence of more Fe^{2+} ions in the solution, which then generated much more $^{\bullet}OH$. Meanwhile, the degradation of MO under acidic conditions was also performed by adding HFZIF-8/GA and different concentrations of H_2O_2, as also shown in Fig. S13b.† Obviously, the absorbance of MO gradually decreased with the increase in H_2O_2 concentration from 0 to 10 mM due to the generation of more $^{\bullet}OH$ in the solution. Thus, it could be concluded that HFZIF-8/GA@HA could degrade in the TME to release Fe^{2+} and GA. At the same time, the self-assembly reaction of Fe^{2+} and GA would form intratumoral Fe-GA complexes. As shown in Fig. S14,† the decrease in MO absorbance indicated the production of hydroxyl radicals, demonstrating that the degradation of HFZIF-8/GA in acidic conditions can release more Fe^{2+} ions.

Next cyclic voltammetry (CV) was performed. When first swept from +1.4 to −0.5 V, no discernible decrease in the peaks was seen. This demonstrated that the electron delocali-

zation effect of Fe-GA endowed these metal sites with enhanced reducibility, whereby they could not further accept electrons from the external environment (Fig. S15a and S15b†). Chronoamperometry (CA) is another method that was used to further evaluate the redox capability of GA-Fe. By analyzing the responses to a limited current, it is possible to transition between two step voltages to favor redox coupling. The finite current response of GA-Fe complex in the CA test was different from that of Fe^{2+} alone, which proved the existence of a metal–ligand interaction (Fig. S15c†). This process corresponds to a chemical reaction proposed in the literature in which GA-Fe acts as an electron donor and is oxidized.[19] Thus, Fe-GA can act as excellent reductive species to catalyze H_2O_2 breakdown to generate $^{\bullet}OH$ (formula (1)).

$$\text{M-GA} + H_2O_2 \rightarrow {}^{\bullet}OH \quad (1)$$

The exchange interaction of Fe ions and the ligand cause a strong electronic delocalization throughout the whole complex, and GA thus becomes a great electron donor.[19] Then the electrons transfer from GA to Fe ions, which can enable the metal ions to change from a high valence state to a low valence state, thus enhancing the CDT by the exchange interaction between Fe ions and the GA ligand (formula (2)). GA^{4-} is finally converted to $GA_{ox}{}^{2-}$ after losing two electrons continuously (formula (3)).

$$GA^{4-}\text{-}e^- \rightarrow GA^{\bullet 3-} \quad (2)$$

$$GA^{\bullet 3-}\text{-}e^- \rightarrow GA_{ox}{}^{2-} \quad (3)$$

As shown in Scheme 1, there are two valence states of Fe^{3+}/Fe^{2+} in the complex. During the Fenton reaction, GA enhances CDT by providing electrons to convert high valence Fe^{3+} into Fe^{2+} to complete the redox cycle of Fe^{3+}/Fe^{2+}. Compared with HFZIF-8, HFZIF-8/GA could produce more $^{\bullet}OH$ under acidic conditions, which proved that Fe-GA had a better $^{\bullet}OH$-generation ability than Fe^{2+} ions (Fig. S16†).

According to above results, the nanozyme catalyzed H_2O_2 to generate a large amount of $^{\bullet}OH$, then TMB was oxidized to form blue oxidized TMB (ox TMB) with typical absorbance at 370 and 652 nm.[54] Interestingly, after the PBS solution (pH 6.5) containing HFZIF-8/GA and H_2O_2 was degraded for 3 h, TMB was added to the above solution and a significant color reaction was observed at room temperature. When the color of the mixed solutions gradually appeared blue from colorless, two significant characteristic peaks could be observed in the UV–vis absorption spectrum (Fig. 2d). As a result, in the presence of H_2O_2, $^{\bullet}OH$ generated by the reaction with Fe ions could further catalyze TMB to produce blue ox TMB, which proved that HFZIF-8/GA has the ability to undergo the Fenton reaction. To reveal the process of $^{\bullet}OH$ generation, 5,5-dimethyl-1-pyrroline oxide (DMPO) was used as a trapping agent for electron spin resonance (ESR) spectroscopy analysis. The distinctive 1 : 2 : 2 : 1 signal appeared in the ESR spectrum when HFZIF-8/GA was introduced in to the PBS solution (pH 6.5, 10 mM GSH) containing 1 mM H_2O_2 for 10 min, which demonstrated the efficient production of $^{\bullet}OH$ with the extension of time (Fig. 2e).

Intratumoral degradation self-assembly

According to the particular responsive degradation of HFZIF-8 in the simulated TME in acidic conditions, the relative release rates of Zn^{2+} and Fe^{2+} ions were tested by inductively coupled plasma atomic emission spectrometry (ICP-OES). After 20 h of degradation in an acidic environment of pH 6.5, the final release rate of Zn^{2+} ions reached 88.79%, while the final release rate of Fe^{2+} ions reached 89.76%. However, the release efficiency of Zn^{2+} ions only reached 14.06% in the simulated normal physiological conditions at pH 7.4, while the release efficiency of Fe^{2+} ions also only reached 29.15% (Fig. 2f and g).

To further observe the degradation behavior of HFZIF-8/GA@HA in acidic conditions after up to 3 h, the morphology of the degradation products was characterized by SEM and TEM. It was found that the degraded cube structure of HFZIF-8/GA@HA was completely destroyed, and small-sized nanoparticles were found in the TEM image of HFZIF-8/GA@HA after being degraded (Fig. S17†). The Bio-TEM picture was analyzed to determine if the cancer-specific M-GA production reactions occur in cancer cells after incubation. With 1 h HFZIF-8/GA@HA incubation, it could be observed that HFZIF-8/GA@HA was successfully taken in to cells (Fig. 2h). Remarkably, when part of the HFZIF-8/GA@HA was broken down after a 12 h incubation with the material, a significant number of solid nanoparticles were generated (Fig. 2i), indicating the feasibility of converting HFZIF-8/GA@HA to Fe-GA in the TME. As shown in Fig. S18,† it could be observed that the lattice spacing (0.25 nm) of Fe-GA was almost equal to that of the complex seen in the TEM image for HFZIF-8/GA@HA after being degraded for 12 h (0.24 nm), while the lattice spacing of Zn-GA was 0.39 nm. Also, it could be observed from the TEM images that the size of HFZIF-8/GA@HA after being degraded for 12 h was about 10 nm, which was significantly different from the morphology of Zn-GA, while the morphology and size of the Fe-GA nanoparticles were very close to those of the degraded complexes. At the same time, the color of the degraded HFZIF-8/GA@HA was obviously blackened, which indicated that the GA coordination competitiveness of Fe^{2+} was much stronger than that of Zn^{2+} (Fig. S19†). Therefore, we could conclude that the complexes in the HR-TEM images of HFZIF-8/GA@HA should be Fe-GA.

Photothermal catalytic therapy with HFZIF-8/GA@HA degradation products

In the acidic environment (pH 6.5), it was found that the degradation products had obvious absorption in the 1064 nm region in the UV–vis absorption spectrum, indicating that the degradation products had NIR-triggered photothermal conversion capability after degradation. At the same time, to test the *in vitro* photothermal conversion performance of HFZIF-8/GA in aqueous solution, the temperature of the different solutions was recorded under continuous laser irradiation for 10 min until the temperature of the solution stabilized (Fig. 3a).[55,56] The temperature of the HFZIF-8/GA nanoparticle solution with

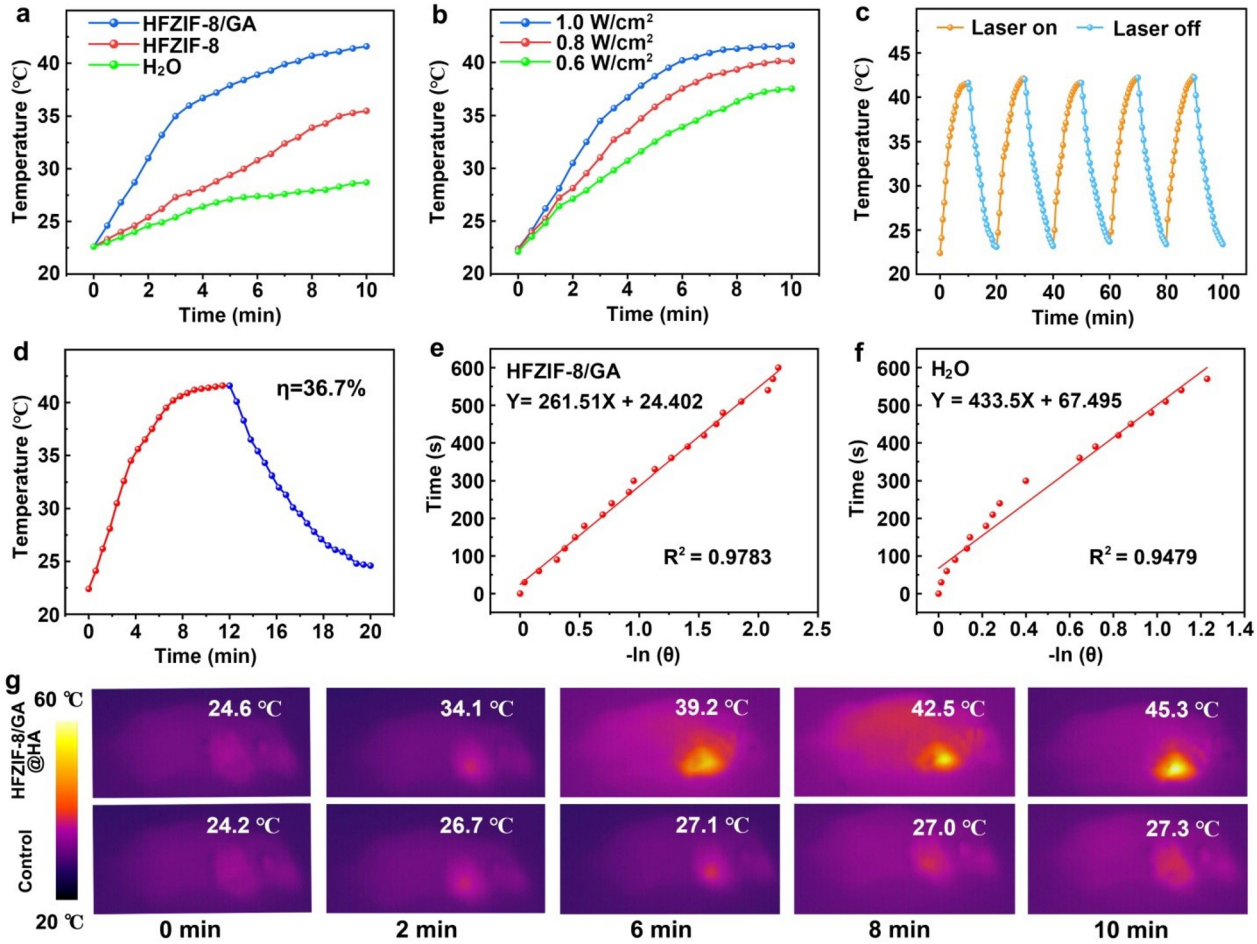

Fig. 3 Temperature changes of the HFZIF-8/GA degradation products, HFZIF-8, and H_2O under 1064 nm laser irradiation (1064 nm, 1.0 W cm^{-2}) for 10 min (pH 6.5) (a). Temperature change curves of HFZIF-8/GA's (500 μg mL^{-1}) degradation products under irradiation for 10 min with different power intensities (pH 6.5) (b). Photothermal stability tests of HFZIF-8/GA (500 μg mL^{-1}) under 1064 nm laser irradiation (1.0 W cm^{-2}) after degradation (pH 6.5) (c). Heating–cooling cycles of HFZIF-8/GA (500 μg mL^{-1}) after degradation in aqueous solution (d). Time *versus* the temperature negative natural logarithm in HFZIF-8@GA (e) and H_2O (f) from the corresponding cooling tests, respectively. Thermal images of U14 tumor-bearing mice in different groups after 10 min NIR-II laser irradiation (g).

a concentration of 1 mg mL^{-1} increased to 43 °C after 10 min illumination. Next, a temperature variation curve of HFZIF-8/GA (1 mg mL^{-1}) under 1064 nm laser with different power densities (0.6, 0.8, 1.0 W cm^{-2}) was plotted,[57] and it could be seen that with the increase in laser power density, the temperature of HFZIF-8/GA aqueous dispersion also increased, and the highest temperature reached 43.6 °C under the irradiation of the 1064 nm laser (1.0 W cm^{-2}), which provides the possibility for *in vivo* antitumor application *via* PTT (Fig. 3b). As revealed in the UV–vis absorption spectrum of MB (Fig. S20†), the absorbance at 43 °C was lower than that at 37 °C, confirming that the photothermal performance could speed up the Fenton reaction rate. In addition, the temperature of pure H_2O increased slightly after 1064 nm laser irradiation for 10 min, and the corresponding temperature variation was about 6.1 °C. It also proved that the material had a photothermal effect. The temperature changes at two different pH values prove the pH-dependent photothermal conversion nature of HFZIF-8/GA (Fig. S21†).

As shown in Fig. 3c, during five heating–cooling cycles, the heating trend of the degradation products was basically the same, confirming the degradation products had good photothermal stability. Meanwhile, photothermal conversion efficiency of the degradation products was further studied (Fig. 3e). After that, the negative natural logarithm data for the time and temperature of degradation (Fig. 3e) and for the H_2O (Fig. 3f) were obtained from a 10 min cooling temperature detection. The corresponding images of HFZIF-8/GA and pure H_2O are shown in Fig. S22–S24.† The photothermal conversion efficiency of the degradation products of HFZIF-8/GA was calculated to be about 36.7%. As displayed in Fig. 3g, a slight temperature change (only 10.1 °C) was observed in the control group using a thermal imager under 10 min laser irradiation, while the highest temperature of the tumor site of the mice treated with HFZIF-8/GA reached 45.3 °C after illumination, indicating that the degradation products of HFZIF-8/GA had a good photothermal property *in vivo*.

In vitro biocompatibility and cytotoxicity against cancer cells

Considering the good CDT and PTT performance of the HFZIF-8/GA@HA nanoparticles, the biocompatibility and cytotoxicity of the HFZIF-8/GA@HA nanoparticles *in vitro* were further studied by the 4,5-dimethylthiazol2-yl-2,5-diphenyl tetrazolium bromide (MTT) method. As displayed in Fig. S25,† when the concentration of HFZIF-8/GA@HA was varied from 0 to 500 μg mL^{-1}, the survival rate of L929 in all the groups was higher than 93.2%, indicating that HFZIF-8 had good biocompatibility for normal cells. Furthermore, the synergistic killing effects of CDT and PTT mediated by HFZIF-8/GA@HA for HeLa cells were explored. The viabilities of HeLa cells treated with HFZIF-8@HA and HFZIF-8/GA@HA are displayed in Fig. 4a. The viability of HeLa cells was more than 50% survival in the HFZIF-8@HA group. By contrast, the survival rates of HeLa cells in the HFZIF-8/GA@HA group decreased rapidly with the increase in HFZIF-8/GA@HA (0–500 μg mL^{-1}) concentration, which could be ascribed to the large amount of $^{\bullet}OH$ produced by the Fe-GA-mediated CDT reaction. When only HFZIF-8/GA@HA was added without another treatment, the viability of HeLa cells was 42.5% at the concentration of HFZIF-8/GA@HA of 500 μg mL^{-1}. When HeLa cells were treated with HFZIF-8/GA@HA and irradiated with a 1064 nm laser (1.0 W cm^{-2}), the cell viability was reduced to 15.4%. The above results indicate that HFZIF-8/GA@HA combined with 1064 nm laser irradiation could efficiently induce cancer cell death, which was attributed to the synergistic effect of PTT and CDT.

The intracellular uptakes of HFZIF-8/GA and HFZIF-8/GA@HA were measured in HeLa cells by confocal laser scan-

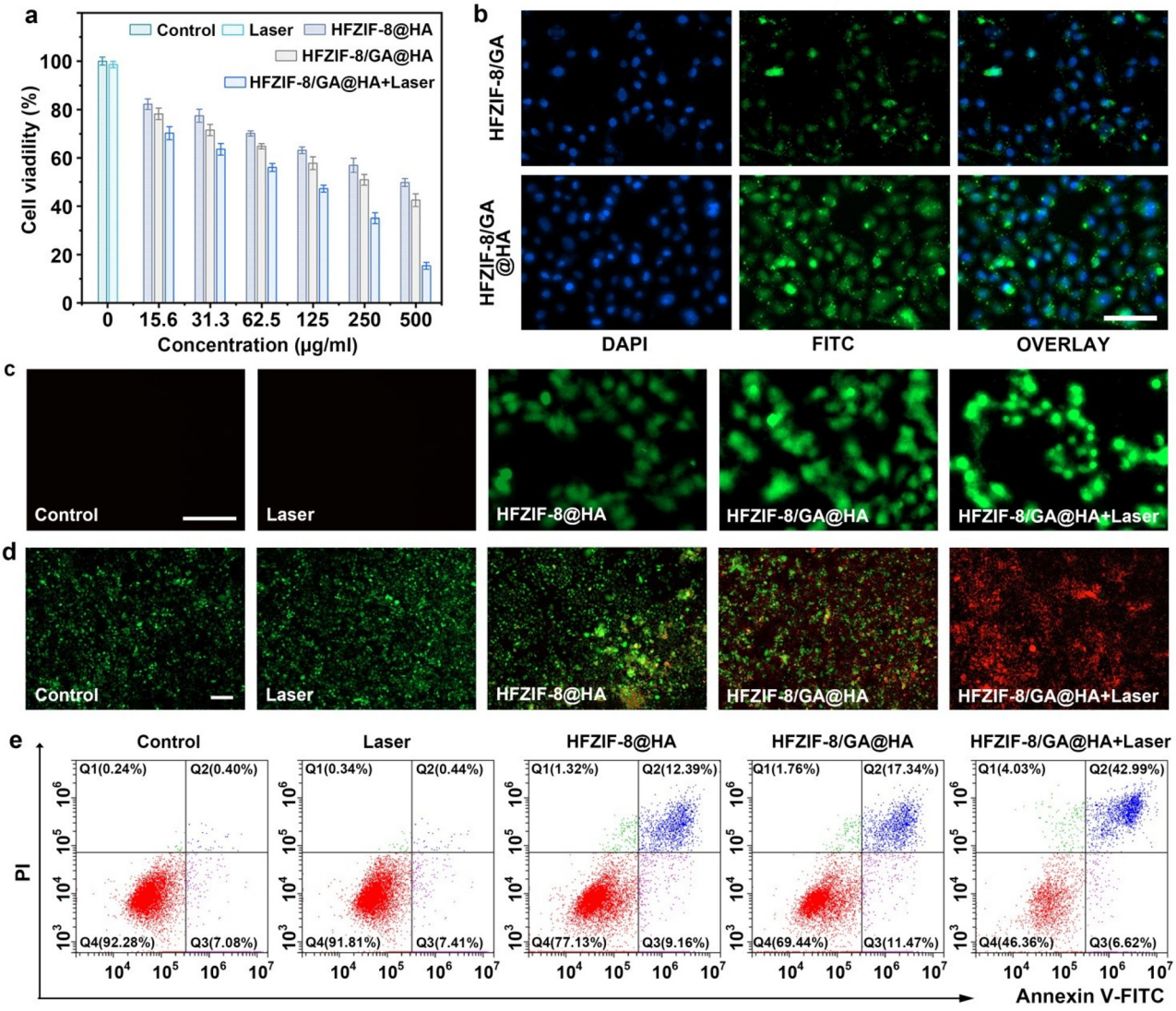

Fig. 4 Viabilities of HeLa cells in the control group, and the groups treated with a 1064 nm laser, HFZIF-8@HA, HFZIF-8/GA@HA, HFZIF-8/GA@HA plus 1064 nm laser (1.0 W cm^{-2}, 10 min) (a). CLSM images of HeLa cells incubated with DAPI and FITC-decorated HFZIF-8/GA@HA for 1 h (b) (scale bar: 100 μm). Detection of intracellular ROS with DCFH-DA (c) (scale bar: 100 μm). Calcein-AM/PI staining images of HeLa cells (d). Flow cytometry investigating of HeLa cells stained by Annexin-FITC/PI at different treatments (e) (scale bar: 200 μm).

ning microscopy (CLSM). Compared to FITC-labeled HFZIF-8/GA, the fluorescence signal of HeLa cells treated with FITC-labeled HFZIF-8/GA@HA was significantly improved (Fig. 4b). In order to further understand the killing mechanism of HFZIF-8/GA@HA on cancerous cells, ROS production mediated by different groups, namely the control, 1064 nm laser, HFZIF-8@HA, HFZIF-8/GA@HA, and HFZIF-8/GA@HA plus 1064 nm laser groups, was detected by the intracellular 2,7-dichlorohydrofluorescein diacetate (DCFH-DA) probe, as DCFH can be oxidized by ROS and produce a green fluorescence signal. Here, no obvious green fluorescence was observed in the control group and the 1064 nm laser group, which proved the negligible ROS in these two groups. Compared to control, 1064 nm laser, and HFZIF-8@HA groups, cells incubated with HFZIF-8/GA@HA or HFZIF-8/GA@HA plus 1064 nm laser irradiation showed stronger fluorescence intensity due to there being more ROS generation caused by the Fenton reaction of Fe-GA (Fig. 4c).

To further detect the antitumor effect of HFZIF-8/GA@HA, calcein-AM and propidium iodide (PI) were used to stain live cells and dead cells for live/dead cell testing. It was worth noting that after CDT (HFZIF-8/GA@HA) treatment, cell death increased dramatically; for the PTT and CDT synergistic treatment (HFZIF-8/GA@HA plus 1064 nm laser) group, almost all the cells died after irradiation (Fig. 4d). Obviously negligible cell death could be found in the control, 1064 nm laser, and HFZIF-8@HA (500 μg mL^{-1}) treatment groups. Next, mitochondrial membrane potential changes were detected by 1,1′,3,3′-tetraethylimidazolium carbocyanine (JC-1) staining in cell experiments; whereby JC-1 exhibits green fluorescence in damaged mitochondria but red fluorescence as an aggregate in healthy mitochondria. Here, the strongest red fluorescence

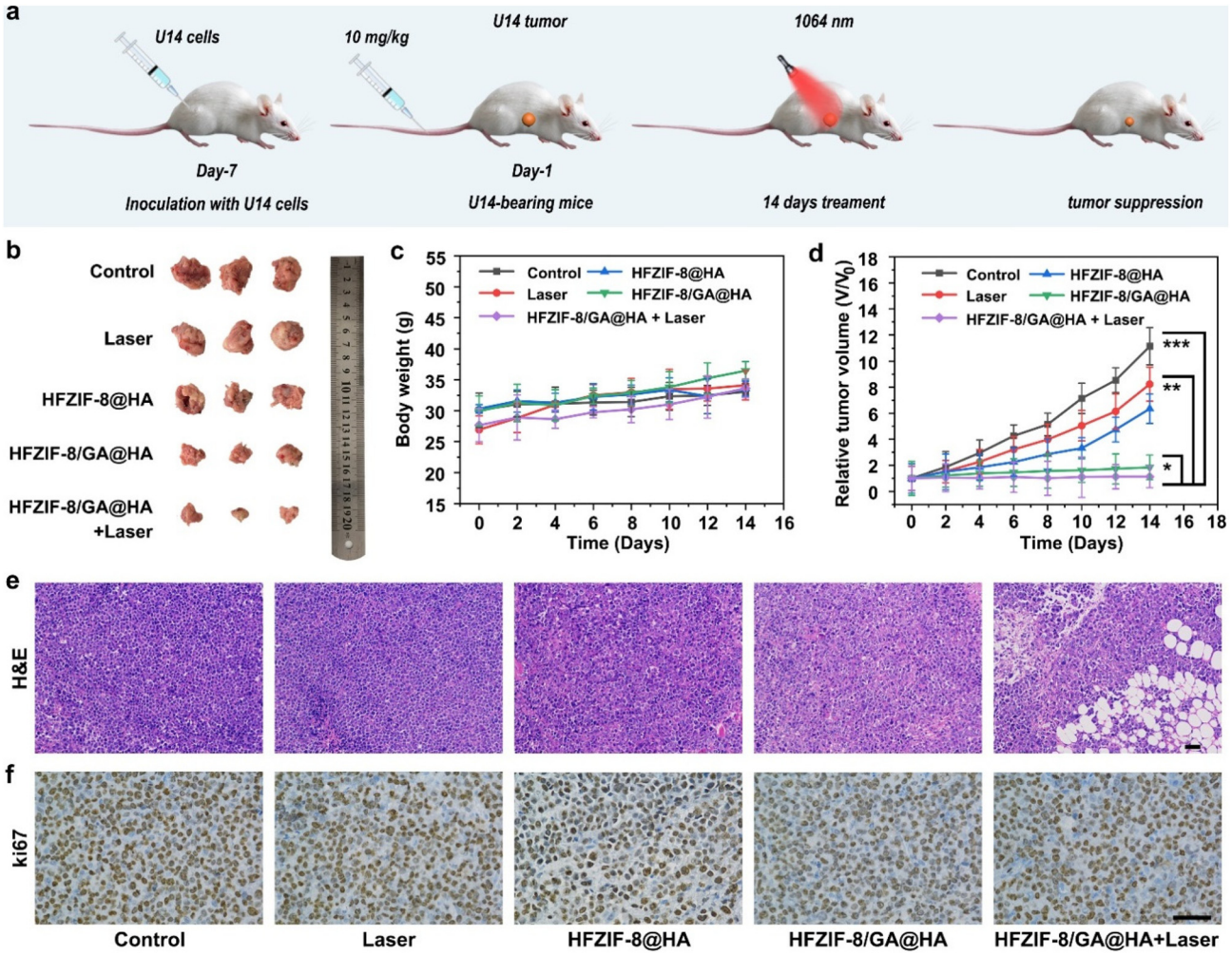

Fig. 5 Schematic illustration of the therapeutic outcome of HFZIF-8/GA@HA administrated by injection in U14-tumor-bearing mice (a). Photographs of dissected tumors from different treatments (b), body weight changes, (c) and the relative tumor volume (d) of the tumor-bearing mice at 14 days. H&E- (e) and Ki67-stained (f) images of tumor tissues in the control, 1064 nm laser, HFZIF-8@HA, HFZIF-8/GA@HA, and HFZIF-8/GA@HA plus 1064 nm laser groups after 14 days therapy (scale bar: 50 μm). Error bars denote the standard deviation (n = 5, mean ± SD, *p < 0.05, **p < 0.01, ***p < 0.001).

signal existed in the control group and the 1064 nm laser group, indicating that there was no damage to the mitochondrial integrity in those groups. As envisioned, the green fluorescence signal observed in the HFZIF-8/GA@HA group was the strongest, indicating that HFZIF-8/GA@HA could effectively damage the mitochondria of cancer cells after laser irradiation (Fig. S26†).[58] In addition, Annexin V-FITC/PI double staining was utilized to analyze the death rate of HeLa cells after different treatments. This also proved that when HeLa cells were incubated with HFZIF-8/GA@HA and irradiated by a 1064 nm laser, most of the cells (≈43%) died (Fig. 4e).

In vivo antitumor efficacy

Using U14 tumor-bearing mice models, *in vivo* antitumor experiments for HFZIF-8/GA@HA were systematically studied by intravenous injection based on satisfactory results at the cellular level. First, five groups of tumor-bearing rats were randomly assigned to various treatment conditions, namely the control, 1064 nm laser irradiation only, HFZIF-8@HA, HFZIF-8/GA@HA, HFZIF-8/GA@HA plus 1064 nm laser irradiation, to assess the effects of anticancer therapy (Fig. 5a). As shown in Fig. 5b, photographs of dissected tumors from different treatments were collected and are displayed. Obviously, compared with the control and 1064 nm laser groups, HFZIF-8@HA had a certain tumor suppression effect. As expected, the HFZIF-8/GA@HA plus laser irradiation group showed the highest effect of inhibiting tumor growth because of the synergistic effect of PTT and CDT.

Also, the body weights and tumor volumes of the mice were recorded during the 14 days treatment period to assess the biosafety and therapy outcome (Fig. 5c). The weight of the animals in the other groups was normal and only slightly increased over the extended period of time, in contrast to the control and 1064 nm laser groups. The results proved that the treatments had no negative effects on the mice's health. Fig. 5d shows the relative tumor volumes of the mouse models, and the results demonstrated that there was a limited inhibitory effect on tumor growth in the HFZIF-8@HA and HFZIF-8/GA@HA groups. Tumor inhibitory effects were significantly more evident for the HFZIF-8/GA@HA group with 1064 nm laser irradiation; this was likely due to the increased $^{\bullet}OH$ production during the thermocatalytic treatment process. Besides, the hematoxylin and eosin (H&E) stained images of the main organs (Fig. S27†), including heart, liver, spleen, lung, and kidney, showed no phenomenon of inflammation or injury, demonstrating the ideal histocompatibility of HFZIF-8/GA@HA. To evaluate the tumor-targeted delivery of HFZIF-8/GA@HA, the *in vivo* bio-distribution of Fe and Zn element and photothermal effects of HFZIF-8/GA were analyzed, and the results are displayed in Fig. S28a, b and S29,† respectively. Taken together, it could be found that the high accumulation of HFZIF-8/GA@HA in tumors could last more than 24 h, which proved the targeting nature of the sample.

Representative tumor tissues of different experimental groups were analyzed by H&E staining to determine the degree of destruction of tumor cells. In accordance with the above results, the H&E staining images of the tumor sections verified that the HFZIF-8/GA@HA plus 1064 nm laser treatment caused the highest damage level to tumor cells (Fig. 5e). As shown in the Ki67-stained tumor tissue sections, compared with other groups, fewer living cells were found in the HFZIF-8/GA@HA plus 1064 nm laser group (Fig. 5f), which further validated that HFZIF-8/GA@HA possessed the highest antitumor effect due to a hyperthermia-enhanced catalytic therapy effect. To further evaluate the *in vivo* biocompatibility of HFZIF-8/GA@HA, blood biochemistry analysis (Table S1†) was performed at different time durations (0, 6, 12, and 24 h), which together with part of the above results proved the excellent biosafety of our developed HFZIF-8/GA@HA nanodrugs.

Conclusions

In summary, a natural TA-tailored hollow mesoporous ZIF-8 with Fe doping, GA loading, and HA modification was prepared for the tumor-targeted delivery of GA and Fe ions, thereby realizing intratumoral coordination electron delocalization-enabled thermocatalytic therapy. Fe doping integrated with TA etching ensured abundant coordination sites and a huge loading space of ZIF-8 for GA loading, and thus the loading rate reached as high as 23.4 wt%. The modification of HA and the nanosize-mediated enhanced permeation and retention effect endowed the HFZIF-8/GA@HA with a tumor selective accumulation nature. Fascinatingly, benefiting from the competitive protonation and coordination capability of tumor-overexpressed protons and metal ions, HFZIF-8/GA@HA can degrade within TME and release Fe ions and GA for intratumoral Fe-GA complex formation. Owning to the unique electron distribution on GA, the coordinated polyhydroxyls could be assisted by conjugated electrons on the benzene ring to form highly stable Fe-GA nanochelates. The electron delocalization effect between Fe ions and GA afforded Fe-GA, which displayed a high photothermal conversion efficiency (η = 36.7%) of 1064 nm NIR-II light for PTT, and thermal energy for accelerated CDT derived from the Fe-mediated Fenton reactions, which was already promoted by the coordination electron delocalization effect of GA. Overall, our work provides a novel strategy to achieve a highly efficient delivery of metal–polyphenol coordination complexes to the TME for PTT-enhanced catalytic therapy.

Experimental

Synthesis of ZIF-8

First, 2 mL of distilled water was mixed with 60 mg of Zn $(NO_3)_2{\cdot}6H_2O$, and 2 mg of CTAB. Then, the above solution was added to 14 mL deionized water containing 908 mg of 2-MeIM, and the mixture was stirred at room temperature for 2 h. Finally, ZIF-8 was harvested from the solution by centrifu-

gation and washed three times with deionized water and methanol alternately.

Synthesis of Fe-doped ZIF-8 (FZIF-8)

First, 2 mL of distilled water was mixed with 40 mg of Zn $(NO_3)_2{\cdot}6H_2O$, 19.5 mg of $FeSO_4{\cdot}7H_2O$, and 2 mg of CTAB, and then the above solution was added to 14 mL of deionized water containing 908 mg of 2-MeIM and the mixture was stirred at room temperature for 2 h. Finally, FZIF-8 was harvested from the solution by centrifugation and washed three times with deionized water and methanol alternately.

Synthesis of hollow FZIF-8 (HFZIF-8)

First, 20 mg of FZIF-8 was dispersed in 3 mL deionized water under ultrasound for 0.5 h at room temperature. After forming a homogeneous dispersion, 2 mL aqueous solution of tannic acid (150 mM) was added and the mixture was stirred for 2 h at room temperature. The obtained HFZIF-8 was centrifuged and lyophilized under vacuum for 6 h.

Preparation of ZIF-8 loaded GA (ZIF-8/GA)

First, 50 mg of ZIF-8 was dispersed in 20 mL of distilled water and sonicated for 1 h. Subsequently, 20 mL GA aqueous solution (600 mM) was slowly mixed into the above solution. Then, the reaction mixture was stirred in the dark at room temperature for 1 h. Finally, ZIF-8/GA was obtained by washing with deionized water and anhydrous ethanol alternately three times. Meanwhile, a brown–black precipitate was collected and vacuum freeze-dried for 6 h.

Preparation of HFZIF-8 loaded GA (HFZIF-8/GA)

First, 50 mg of HFZIF-8 was dispersed in 20 mL of distilled water and sonicated for 1 h. Subsequently, 20 mL of GA aqueous solution (600 mM) was slowly mixed into the above solution. Then, the reaction mixture was stirred in the dark at room temperature for 1 h. Finally, HFZIF-8/GA was obtained by washing with deionized water and anhydrous ethanol alternately three times. Subsequently, a brown–black precipitate was collected and vacuum freeze-dried for 6 h.

Modification of HFZIF-8/GA with hyaluronic acid (HA)

First, 50 mg of HFZIF-8/GA was dispersed in 40 mL of deionized water and sonicated for 0.5 h. Then, 10 mL of HA aqueous solution (2 mM) was mixed with the above solution and stirred at 60 °C for 12 h. Finally, HFZIF-8/GA@HA was obtained by washing the product three times with deionized water, collecting a brown–black precipitate, which was vacuum freeze-dried for 6 h. FITC was used to modify HFZIF/GA@HA, denoted as FITC-modified HFZIF/GA@HA.

Live subject statement

All animal procedures were performed in accordance with the Guidelines for Care and Use of Laboratory Animals of the Drug Safety Evaluation Center of Harbin Medical University (no. SYDW 2019-82) and approved by the Animal Ethics Committee of The Second Affiliated Hospital of Harbin Medical University.

Author contributions

Xing Yang: investigation, methodology, writing– original draft. Chunsheng Li: writing – review & editing. Shuang Liu: data analysis. Yunlong Li: writing – review & editing. Xinyu Zhang: data analysis. Qiang Wang: writing – review & editing. Jin Ye: data analysis, writing – review & editing. Yong Lu: data analysis. Yujie Fu: resources, funding acquisition. Jiating Xu: supervision, conceptualization, funding acquisition, writing – review & editing.

Conflicts of interest

There are no conflicts to declare.

Acknowledgements

Financial support from the National Key Research and Development Program of China (2022YFD2200602), 111 Project (B20088), National Natural Science Foundation of China (52202345 and 31930076), and the Heilongjiang Touyan Innovation Team Program (Tree Genetics and Breeding Innovation Team) are greatly acknowledged. The authors want to thank Shiyanjia Lab (**https://www.shiyanjia.com**) for the support of HRTEM and elemental mapping tests. The authors would like to acknowledge the technical support from Analysis and Testing Center of Northeast Forestry University. Meanwhile, the authors would like to thank Mitochondrial Membrane Potential Kit (JC-1 Assay) provided by Beijing Solarbio Technology Co., Ltd.

References

1 F. Reitzer, M. Allais, V. Ball and F. Meyer, *Adv. Colloid Interface Sci.*, 2018, **257**, 31–41.
2 Z. Chen, M. A. Farag, Z. Zhong, C. Zhang, Y. Yang, S. Wang and Y. Wang, *Adv. Drug Delivery Rev.*, 2021, **176**, 113870.
3 Z. Zhang, W. Sang, L. Xie, W. Li, B. Li, J. Li, H. Tian, Z. Yuan, Q. Zhao and Y. Dai, *Angew. Chem., Int. Ed.*, 2021, **60**, 1967–1975.
4 M. C. Bonferoni, S. Rossi, G. Sandri and F. Ferrari, *Semin. Cancer Biol.*, 2017, **46**, 205–214.
5 S. Sajadimajd, R. Bahramsoltani, A. Iranpanah, J. Kumar Patra, G. Das, S. Gouda, R. Rahimi, E. Rezaeiamiri, H. Cao, F. Giampieri, M. Battino, R. Tundis, M. G. Campos, M. H. Farzaei and J. Xiao, *Pharmacol. Res.*, 2020, **151**, 104584.
6 O. Olejnik and A. Masek, *Molecules*, 2022, **27**, 2214.

7 T. Liu, W. Liu, M. Zhang, W. Yu, F. Gao, C. Li, S. B. Wang, J. Feng and X. Z. Zhang, *ACS Nano*, 2018, **12**, 12181–12192.
8 Z. Ren, S. Sun, R. Sun, G. Cui, L. Hong, B. Rao, A. Li, Z. Yu, Q. Kan and Z. Mao, *Adv. Mater.*, 2019, **32**, 1906024.
9 H. Wang, D. Wang, H. Huangfu, H. Lv, Q. Qin, S. Ren, Y. Zhang, L. Wang and Y. Zhou, *Mater. Des.*, 2022, **224**, 111401.
10 J. Qin, G. Liang, B. Feng, G. Wang, N. Wu, Y. Deng, A. A. Elzatahry, A. Alghamdi, Y. Zhao and J. Wei, *Chin. Chem. Lett.*, 2021, **32**, 842–848.
11 S. Liu, X. Xu, J. Ye, J. Wang, Q. Wang, Z. Liu, J. Xu and Y. Fu, *Chem. Eng. J.*, 2023, **456**, 140892.
12 A. K. Mittal, S. Kumar and U. C. Banerjee, *J. Colloid Interface Sci.*, 2014, **431**, 194–199.
13 C. Locatelli, F. B. Filippin-Monteiro and T. B. Creczynski-Pasa, *J. Med. Chem.*, 2013, **60**, 233–239.
14 J. Gutiérrez-Fernández, M. R. García-Armesto, R. Álvarez-Alonso, P. del Valle, D. de Arriaga and J. Rúa, *J. Dairy Sci.*, 2013, **96**, 4912–4920.
15 J. Guo, Y. Ping, H. Ejima, K. Alt, M. Meissner, J. J. Richardson, Y. Yan, K. Peter, D. von Elverfeldt, C. E. Hagemeyer and F. Caruso, *Angew. Chem., Int. Ed.*, 2014, **53**, 5546–5551.
16 D. Wu, B. Zhou, J. Li, X. Wang, B. Li and H. Liang, *Adv. Healthcare Mater.*, 2022, **11**, 2200559.
17 M. Zhang, L. Wang, H. Jin, N. Zhao, Y. Liu, S. Lan, S. Liu and H. Zhang, *J. Controlled Release*, 2023, **358**, 612–625.
18 J. X. Fan, D. W. Zheng, W. W. Mei, S. Chen, S. Y. Chen, S. X. Cheng and X. Z. Zhang, *Small*, 2017, **13**, 1702714.
19 B. Yang, H. Yao, H. Tian, Z. Yu, Y. Guo, Y. Wang, J. Yang, C. Chen and J. Shi, *Nat. Commun.*, 2021, **12**, 3393.
20 X. Sun, S. Zhang, Q. Li, M. Yang, X. Qiu, B. Yu, C. Wu, Z. Su, F. Du and M. Zhang, *J. Colloid Interface Sci.*, 2023, **642**, 691–704.
21 J. H. Park, K. Kim, J. Lee, J. Y. Choi, D. Hong, S. H. Yang, F. Caruso, Y. Lee and I. S. Choi, *Angew. Chem., Int. Ed.*, 2014, **53**, 12420–12425.
22 S. Sharma, D. Mittal, A. K. Verma and I. Roy, *ACS Appl. Bio Mater.*, 2019, **2**, 2092–2101.
23 P. Zhang, Y. Hou, J. Zeng, Y. Li, Z. Wang, R. Zhu, T. Ma and M. Gao, *Angew. Chem., Int. Ed.*, 2019, **58**, 11088–11096.
24 Y. N. Hao, Y. R. Gao, Y. Li, T. Fei, Y. Shu and J. H. Wan, *Adv. Mater. Interfaces*, 2021, **8**, 2101173.
25 C. Liu, C. Li, S. Jiang, C. Zhang and Y. Tian, *Nanoscale Adv.*, 2022, **4**, 173–181.
26 S. Roy, I. Hasan and B. Guo, *Coord. Chem. Rev.*, 2023, **482**, 215075.
27 S. Roy, N. Bag, S. Bardhan, I. Hasan and B. Guo, *Adv. Drug Delivery Rev.*, 2023, **197**, 114821.
28 G. Chong, R. Su, J. Gu, Y. Yang, T. Zhang, J. Zang, Y. Zhao, X. Zheng, Y. Liu, S. Ruan, R. He, W. Yin, Y. Li, H. Dong and Y. Li, *Chem. Eng. J.*, 2022, **435**, 134993.
29 Z. Dong, L. Feng, Y. Chao, Y. Hao, M. Chen, F. Gong, X. Han, R. Zhang, L. Cheng and Z. Liu, *Nano Lett.*, 2018, **19**, 805–815.
30 X. Yu, T. Shang, G. Zheng, H. Yang, Y. Li, Y. Cai, G. Xie and B. Yang, *Chin. Chem. Lett.*, 2022, **33**, 1895–1900.
31 F. Liu, X. He, H. Chen, J. Zhang, H. Zhang and Z. Wang, *Nat. Commun.*, 2015, **6**, 8003.
32 Z. Xie, S. Liang, X. Cai, B. Ding, S. Huang, Z. Hou, P. a. Ma, Z. Cheng and J. Lin, *ACS Appl. Mater. Interfaces*, 2019, **11**, 31671–31680.
33 I. B. Vasconcelos, T. G. d. Silva, G. C. G. Militão, T. A. Soares, N. M. Rodrigues, M. O. Rodrigues, N. B. d. Costa, R. O. Freire and S. A. Junior, *RSC Adv.*, 2012, **2**, 9437–9442.
34 M. Xu, Y. Hu, W. Ding, F. Li, J. Lin, M. Wu, J. Wu, L. P. Wen, B. Qiu, P. F. Wei and P. Li, *Biomaterials*, 2020, **258**, 120308.
35 Q. Wang, Y. Sun, S. Li, P. Zhang and Q. Yao, *RSC Adv.*, 2020, **10**, 37600–37620.
36 Q. Sun, H. Bi, Z. Wang, C. Li, X. Wang, J. Xu, H. Zhu, R. Zhao, F. He, S. Gai and P. Yang, *Biomaterials*, 2019, **223**, 119473.
37 P. Z. Moghadam, T. Islamoglu, S. Goswami, J. Exley, M. Fantham, C. F. Kaminski, R. Q. Snurr, O. K. Farha and D. Fairen-Jimenez, *Nat. Commun.*, 2018, **9**, 1378.
38 C. Li, J. Ye, X. Yang, S. Liu, Z. Zhang, J. Wang, K. Zhang, J. Xu, Y. Fu and P. Yang, *ACS Nano*, 2022, **16**, 18143–18156.
39 C. Zheng, Y. Wang, S. Z. F. Phua, W. Q. Lim and Y. Zhao, *ACS Biomater. Sci. Eng.*, 2017, **3**, 2223–2229.
40 F. Jiang, Y. Zhao, C. Yang, Z. Cheng, M. Liu, B. Xing, B. Ding, P. a. Ma and J. Lin, *Dalton Trans.*, 2022, **51**, 2798–2804.
41 L. Zhang, S. S. Wan, C. X. Li, L. Xu, H. Cheng and X. Z. Zhang, *Nano Lett.*, 2018, **18**, 7609–7618.
42 Z. Wu, L. Wang, S. Chen, X. Zhu, Q. Deng, J. Wang, Z. Zeng and S. Deng, *Chem. Eng. J.*, 2021, **404**, 126579.
43 L. M. Wang, W. Y. Liu, M. L. Hu, J. S. Yao, P. Wang, J. H. Liu, M. He, Y. Gao and Z. X. Li, *Rare Met.*, 2022, **41**, 2701–2710.
44 X. Li, X. Shu, Y. Shi, H. Li and X. Pei, *Chin. Chem. Lett.*, 2023, **34**, 107986.
45 J. W. M. Osterrieth and D. Fairen-Jimenez, *Biotechnol. J.*, 2021, **16**, e2000005.
46 L. Gao, Z. Wu, A. R. Ibrahim, S. F. Zhou and G. Zhan, *ACS Biomater. Sci. Eng.*, 2020, **6**, 6095–6107.
47 S. Li, L. Zhang, X. Liang, T. Wang, X. Chen, C. Liu, L. Li and C. Wang, *Chem. Eng. J.*, 2019, **378**, 122175.
48 M. Kim, X. Xu, R. Xin, J. Earnshaw, A. Ashok, J. Kim, T. Park, A. K. Nanjundan, W. A. El-Said, J. W. Yi, J. Na and Y. Yamauchi, *ACS Appl. Mater. Interfaces*, 2021, **13**, 52034–52043.
49 Q. Fan, J. Zuo, H. Tian, C. Huang, E. C. Nice, Z. Shi and Q. Kong, *J. Exp. Clin. Cancer Res.*, 2022, **41**, 162.
50 Y. Lu, G. Zhang, H. Zhou, S. Cao, Y. Zhang, S. Wang and H. Pang, *Angew. Chem., Int. Ed.*, 2023, **62**, e202311075.
51 J. Cai, J. Fu, R. Li, F. Zhang, G. Ling and P. Zhang, *Carbohydr. Polym.*, 2019, **208**, 356–364.
52 X. Li, Y. Pan, J. Zhou, G. Yi, C. He, Z. Zhao and Y. Zhang, *J. Colloid Interface Sci.*, 2022, **605**, 296–310.

53 R. Wang, J. Shi, L. Song, S. Zheng, X. Liu, M. Hong and Y. Zhang, *Adv. Funct. Mater.*, 2021, **31**, 2106884.
54 Y. Cheng, S. Song, P. Wu, B. Lyu, M. Qin, Y. Sun, A. Sun, L. Mu, F. Xu, L. Zhang, J. Wang and Q. Zhang, *Adv. Healthcare Mater.*, 2021, **10**, 2100590.
55 J. Su, S. Lu, Z. Wei, B. Li, J. Li, J. Sun, K. Liu, H. Zhang and F. Wang, *Small*, 2022, **18**, 2200897.
56 J. Ye, W. Lv, C. Li, S. Liu, X. Yang, J. Zhang, C. Wang, J. Xu, G. Jin, B. Li, Y. Fu and X. Liang, *Adv. Funct. Mater.*, 2022, **32**, 2206157.
57 S. Zhang, W. Guo, J. Wei, C. Li, X. J. Liang and M. Yin, *ACS Nano*, 2017, **11**, 3797–3805.
58 B. Xu, S. Li, L. Zheng, Y. Liu, A. Han, J. Zhang, Z. Huang, H. Xie, K. Fan, L. Gao and H. Liu, *Adv. Mater.*, 2022, **34**, 2107088.